Experimental Investigation of Microencapsulated Phase Change Material Water Slurry Performance in an Oscillating Heat Pipe

---

A Thesis

Presented to

the Faculty of the Graduate School

at the University of Missouri – Columbia

In Partial Fulfillment

of the Requirements for the Degree

Master of Science

---

by

Max Noelker

Professor Hongbin Ma, Advisor and Thesis Supervisor

DECEMBER 2022

The undersigned have examined the thesis entitled

Experimental Investigation of Microencapsulated Phase Change Material Water Slurry Performance in an Oscillating Heat Pipe

presented by Max Noelker

a candidate for the degree of

Master of Science Mechanical & Aerospace Engineering

and hereby certify that in their opinion it is worthy of acceptance.

Professor Hongbin Ma

Professor Gary Solbrekken

Professor Stephen Montgomery-Smith

Acknowledgements

A special thanks to my Mom and Dad for providing me an environment for success and invaluable guidance. I am forever grateful for the sacrifices you have both made to allow for me to succeed and grow as an individual.

Additionally, I want to thank Dr. Hongbin Ma for his willingness to sponsor my research. I appreciate his direction and patience with me as a student, and your contributions to my character will forever benefit me.

I want to thank my colleagues who have assisted my research: Mark Owoola and Dr. Shahabeddin Mohammadian.

Lastly, the project has been partially supported by the Office of Naval Research Grant No. N00014-19-1-2006 directed by Dr. Mark Spector.

Table of Contents

Nomenclature

A – Area [m^2]

C – Thermal Conductance [W/K]

C_p – Specific Heat [J/kg×K]

dT – Temperature Differential [°C or K]

E – Encapsulation Ratio [%]

I – Current [A]

L – Length [m]

k – Thermal Conductivity [W/m×K]

$\dot{m}$ – Mass Flow Rate [kg/s]

P – Power [W]

Q – Power Input [W]

R – Encapsulation Ratio [%]

T – Temperature [°C or K]

$\bar{T}$– Temperature Average [°C or K]

V – Voltage [Volts]

Greek

α – Volume Percentage [%]

ΔH – Latent Heat [J/g]

μ- Dynamic Viscosity [N×s/m]

ϕ - Weight Percentage [%]

ρ – Density [kg/m^3]

Subscripts

c – Condenser

e – Evaporator

eff – Effective Property

m – Melting

MPCM – Micro-encapsulated Phase Change Material

MR – Melting Range

o – Onset Melting

OHP – Oscillating Heat Pipe

PCM – Phase Change Material

s – Solidification

slurry – Slurry

water – Water

List of Tables

List of Figures

Abstract

An experimental investigation was performed to determine the heat transfer performance of an oscillating heat pipe (OHP) with a micro-encapsulated phase change material (MPCM) slurry working fluid. In this investigation, MPCMs with diameters ranging from 3.8 μm to 29.4 μm was added in the working fluid to determine MPCMs' effect on the heat transport capability. It is expected that when the MPCMs are in the evaporator, the MPCMs change phase from solid to liquid to absorb more thermal energy. When the MPCMs move to the condenser section, MPCMs change phase from liquid to solid, the MPCMs can release more thermal energy. In this way, it can help increase the heat transport capability in an OHP. The effects of the encapsulation ratio, encapsulation efficiency, geometric dimensions, density, and latent heat of investigated MPCMs on the thermal performance in OHPs were experimentally conducted. Experimental results show that the MPCMs added in the working fluid can enhance the heat transport capability in an OHP and it is found that the best performance of the OHP occurred at a MPCM weight concentration of 3% in the slurry, which can achieve an improvement of 15.5%.

Chapter I. Introduction

As the electronics and aerospace industries continues to develop new technologies, the amplitude of concentrated heat fluxes continues to increase. These thermal loads demand efficient mitigation solutions. Metal oxide semiconductors produce heat flux of 100 $\frac{W}{cm^2}$ to 200 $\frac{W}{cm^2}$ [1]. Additionally, spacecrafts require strategies to transfer heat concentrations from internal components in microgravity conditions [2-3]. Conventional heat pipes do not effectively transfer heat from areas of concentrated heat and cannot satisfy certain heat transfer requirements. Alternatively, Oscillating Heat Pipes (OHPs) presents a solution to large heat flux because it yields a higher thermal conductivity than conventional heat pipes. The OHP was first introduced into scientific literature by Akachi in 1990 [4]. The OHP is wickless as compared to conventional heat pipes. When power is applied to the evaporating section, the OHP acts as an active cooling device converting heat into phase change and kinetic energy. This motion can be visualized as liquid plugs and vapor bubbles in oscillating motion. Due to the vapor expansion and compression induced from the phase change of the OHP working fluid, a pressure differential produces oscillating motion. To produce liquid plugs and vapor slugs, the OHP channel must be small enough to separate liquid plugs and vapor bubbles using the surface tension produced from the meniscus radius. The liquid plugs and vapor slugs flow unidirectionally, therefore there are little frictional losses between the two phases. The oscillating motion enhances forced convection and phase change heat transfer. As power increases in an OHP, the heat transport capabilities increase as well [5]. If too large a heat flux is applied, then dry-out conditions are achieved in which no oscillations occur. The system of an OHP can be visualized in Fig. 1.1 [6]. Overall,

OHP's have high heat transport capability, low pressure drops, and low manufacturing cost.

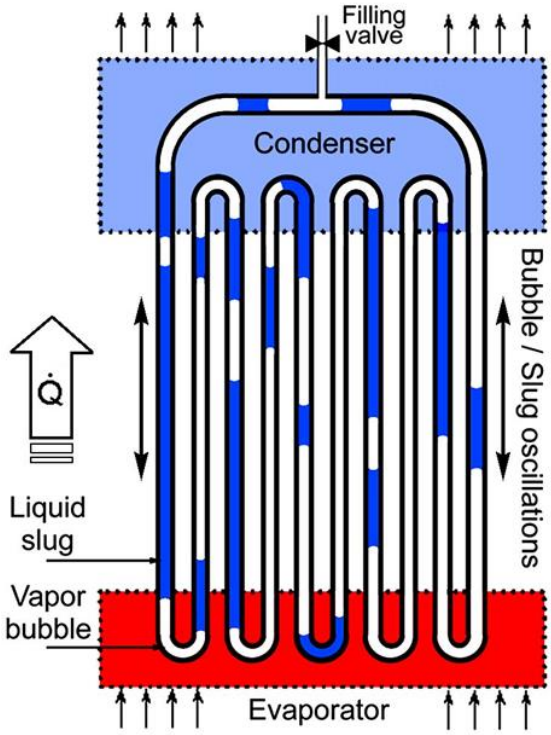

Figure 1.1 Configuration of an OHP [6]

The OHP is partially filled with a working fluid. Working fluid selection is a popular research topic because there are numerous possibilities that reflect unique applications. It has been found that working fluids suspending microparticles and nanoparticles enhance the heat transport capability of a OHP [5]. Ma et al. [7] discovered thermal conductivity can be increased by 40% and 150% if copper nanoparticles or carbon nanotubes are dispersed in ethylene glycol or oil respectively. Typically, with less than 1% of volume fraction of nanoparticles added to working fluids. Working fluids of ethanol or acetone require less power to start oscillating motions in OHP [8]. If a working fluid has a vapor-liquid saturation line with a large slope and a low latent heat,

oscillations will be achieved with smaller heat flux [9-10]. Low latent heats promote low energy evaporation and condensation. If there is a steep vapor-liquid saturation line, then a small increase in temperature will produce a large increase in pressure. Zhou et al. [11] experimentally confirmed a graphene nanofluid working fluid enhances OHP heat transfer. The maximum reduction in thermal resistance was 83.6% for an OHP filled with 2% graphene nanofluid compared to deionized water at a filling ratio of 62% and power of 80W. Additionally, PCM have been introduced outside of OHPs to serve as a thermal battery system [12]. It was determined that the start temperature of the OHP system should be below that of the phase change temperature of the PCM for optimal heat transport [12]. If this in not satisfied, the OHP will not be oscillating during the phase change of the PCM. Wang et al. [12] found a PCM-OHP system was more effective heat transport device than a OHP cooling system. To improve the low thermal conductivities of PCMs, metals with high thermal conductivities can be mixed with PCMs. For example, a graphite paraffin mixture was utilized in an OHP, and performance did not deviate before the melting temperature range [13]. PCM can also be encapsulated by polymer through a chemical synthesis to improve thermal degradation and rigidity characteristics. Adding micro-encapsulated PCMs (MPCMs) to OHP has been seen to improve dry-out capabilities of an OHP [14]. To avoid dry-out, PCMs with an appropriate melting temperature range must be selected. While utilizing a PCM thermal battery on the outside of a closed loop OHP, performance decreases when the PCM phase change is complete [15]. Heydrarian et al. [16] determined nano encapsulated PCMs (NPCMs) decrease the thermal resistance of OHPs and therefore improve heat transfer.

There are many factors that impact the heat transfer performance of an OHP. Filling ratio, the ratio of liquid to vapor in the OHP, is another popular research topic and factor that effects heat transport in an OHP. Typically, a filling ratio is selected between 35-70% dependent upon the working fluid, heat flux, and applications. Too low of a filling ratio produces dry out conditions at lower applied powers. For one application, a filling ratio of 50% is shown to start oscillating before that of a filling ratio of 70% [8]. Another characteristic that effects OHP performance is surface wettability. Hydrophobic means the surface is resistant to wetting, which results in beading up of water and large contact angles. Hydrophilic is attracted to water where a thin film and small contact angle can be produced. A hydrophilic copper OHP improves heat transport capabilities in comparison to a traditional copper OHP [17]. Surface wettability and contact angle influence both slug motion and thermal performance of an OHP [17]. OHP have also been orientated in multiple ways. Predominantly either horizontal or vertical, with the vertical OHP yielding the best heat transfer results.

Overall, OHPs are utilized in a variety of applications. The OHP will continue to increase in use as the manufacturing cost is driven down by mass production. OHPs have been studied as alternatives to conventional heat pipes for solar collector operating systems. OHP in solar operating systems are seen with a thermal efficiency of 62% and are cheaper to manufacture than traditional solar collector operating systems [18]. OHPs have been utilized in aerospace applications where high heat fluxes are present [19]. In hybrid vehicle applications the OHP functioned with high reliability and reproducibility and without failure during start-up or working stage [20].

Heat can be transferred to a PCM as sensible heat and latent heat. Where sensible heat is the heat transferred through a temperature difference in which no phase change occurs. Sensible heat storage mediums typically consist of water, molten slats, sand, or rocks. Sensible heat storage systems offer high thermal conductivities and low cost [21]. Latent heat is the heat transferred through a phase change at a phase change temperature or temperature range. The high latent heats of paraffin waxes offer solutions to thermal engineering problems. In Fig. 1.2 latent heat transfer occurs at a specified melting temperature and absorbs the heat during the phase change.

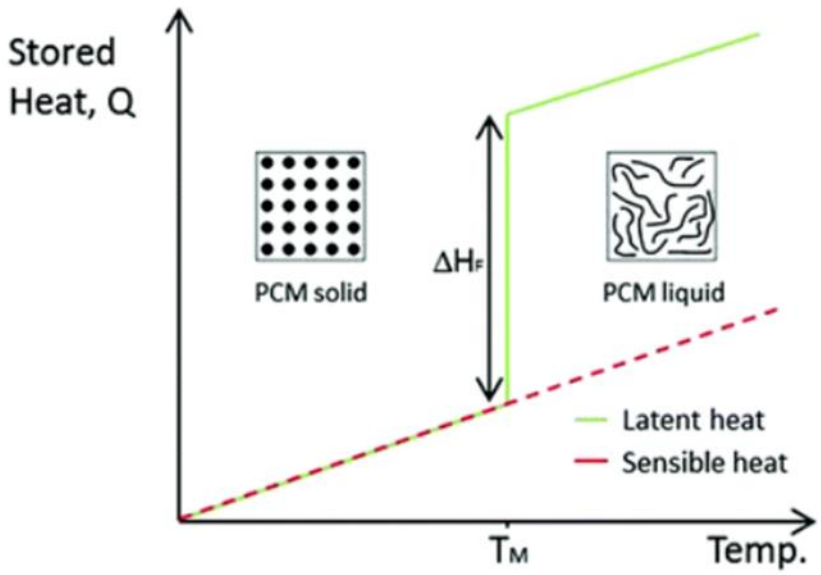

Figure 1.2 Solid-liquid phase change and heat transfer [22].

Paraffin waxes have no phase separation after solid-liquid transition, low vapor pressure, but it has a low thermal conductivity of 0.2 $\frac{W}{m\times K}$[23]. Additionally, paraffin waxes offer melting temperatures over a large range of temperatures. Therefore, paraffin waxes can be specialized for different temperature applications. MPCMs offer benefits

over regular PCMs by enhancing thermal and mechanical performance of PCMs used in thermal energy storage by increasing the heat transfer area and preventing leakage of melting materials [24]. Additionally, MPCMs low density allow for easy suspension of the microparticles while acting as a solute in liquids. Regular PCMs diffuse to surfaces gradually [24]. MPCMs high latent heat, low density, mechanical rigidity, and large surface can enhance heat transfer of an OHP when concentrated in the working fluid.

Utilizing the surface tension and meniscus radius at the liquid-vapor interface, an OHP can form a train of liquid plugs and vapor bubbles. With the thermally excited oscillation and phase change heat transfer, an OHP can effectively integrates extra-high performance of thin-film evaporation, vortex heat transfer enhancement, momentum overshoot near the capillary wall, entrance region effect, and two-phase heat transfer in a capillary, resulting in an extra-high heat transport capability. In order to further increase the heat transport capability in an OHP, in this investigation, MPCMs with diameters ranging from 3.8 μm to 29.4 μm is added in the working fluid. The MPCM phase change temperature should be between the condensation and evaporation temperature. When the MPCMs are in the evaporator, the MPCMs change phase from solid to liquid to absorb more thermal energy. When the MPCMs move to the condenser section, MPCMs change phase from liquid to solid, the MPCMs can release more thermal energy. In this way, it can help increase the heat transport capability in an OHP through both sensible heat and latent heat. In addition, it is expected that MPCMs offer additional effect of particle's oscillation turbulence in the thermal boundary in the capillary tubing similar to nanoparticles effect in an OHP [25-28].

Chapter II. MPCM/PCM Characterization

2.1 DSC Procedure

To begin a DSC experiment, the gas valve was first opened to the nitrogen chamber. Turn the DSC on from the switch in the back of the system. Turn on the RCS Chiller to ensure for temperature regulation of the system. In the TA Instrument Explorer window, select the Q20 icon with your cursor. In the Q20 window select, 'Control', 'Event', and 'On to turn on RCS (chiller)'. Next the sample of focus must be prepared. The sample should be a dry sample and heat overnight to remove moisture if necessary. Place the pan with the lid included on the scale and zero the scale. Remove the pan and place your sample into the pan and record the mass of the sample read on the scale. This value can vary from 5 – 15 mg. Place the lid onto the pan and crimp the lid on firmly to the pan using the crimp machine. Then you must place the sample into the DSC by removing the outer lid and carefully removing the inner lid with tweezers. Then remove the second inner lid with tweezers as well and do not move the empty reference pan with lid. Carefully place your sample pan on the opposite side of the platform utilizing tweezers. Place all three lids back to their original positions. Click on 'Experiment' on the left toolbar display the last experiment sequence. In the 'Summary' tab select the desired testing format. Input the sample name, pan type, sample size, any comments, and choose a location to save your data. In the 'Procedure' tab, input the temperature and heating rate parameters that are appropriate for your run. A common heating rate is $10\,\frac{℃}{min}$. A common strategy for a phase change material is select an upper and lower temperature bounds centered around the phase change and at least 5°C before and after onset and offset temperatures respectively. In notes ensure that nitrogen is selected at the

purge gas and the flow rate is set to 50 $\frac{mL}{min}$. Click the ‘Apply’ button to update the experimental sequence. Click on the ‘Run’ button to begin your experiment. Data Analyzation is utilized in ‘Plot View’ or ‘Full Size Plot View’ icon on the top of the toolbar to display the window in the center. Open the DSC curve, use the top toolbar to annotate the graph with important values. Choose ‘Files’, ‘Export PDF’. After the experiment ends, turn off the RCS, ‘Control’, ‘Event’, ‘Off’. Close the Q20 software and turn off the DSC.

2.2 DSC Results

Digital Scanning Calorimeter (DSC) testing was conducted to determine the latent heat of melting and solidification, onset temperatures, offset temperatures, and melting/solidification temperatures for the MPCMs and PCMs samples from Microtek Laboratories, Inc. By integrating over the endotherms and exotherms latent heat of melting and solidification can be calculated. TA Universal Software Analysis was utilized to integrate across Figs. 2.2.1 - 2.2.2. Endothermic curves are representative of a response in which melting occurred. Exothermic curves are representative of a response in which solidification occurred. The melting temperature of Nexttek37D is advertised as 35°C – 39°C on the safety data sheet (SDS). The Nexttek37D melting temperature in Fig. 2.2.1(a) is 38.33°C. The onset temperature for Nexttek37D melting is 20°C and the offset temperature is 52°C. The melting temperature of PCM37 is 39.47°C in Fig. 2.2.1(a). The polymer shell on the Nexttek37D decreases the latent heat of melting of the PCM37 by 29.31%. The solidification temperature of the Nexttek37D begins at the at 19.62°C as seen in Fig. 2.2.1(b). The onset temperature for Nexttek37D solidification in Fig. 2.2.1(b) is 10°C and the offset temperature is 40°C. The solidification temperature of PCM37 is

24.94°C. The onset temperature for PCM37 solidification in Fig. 2.2.1(b) is 10°C and the offset temperature is 35°C. The odd curvature of the response seen in Fig. 2.2.1(b) is most likely due to decomposition of the PCM37, this meaning when mass leaves the system, there is an impulse of heat flow out of the system.

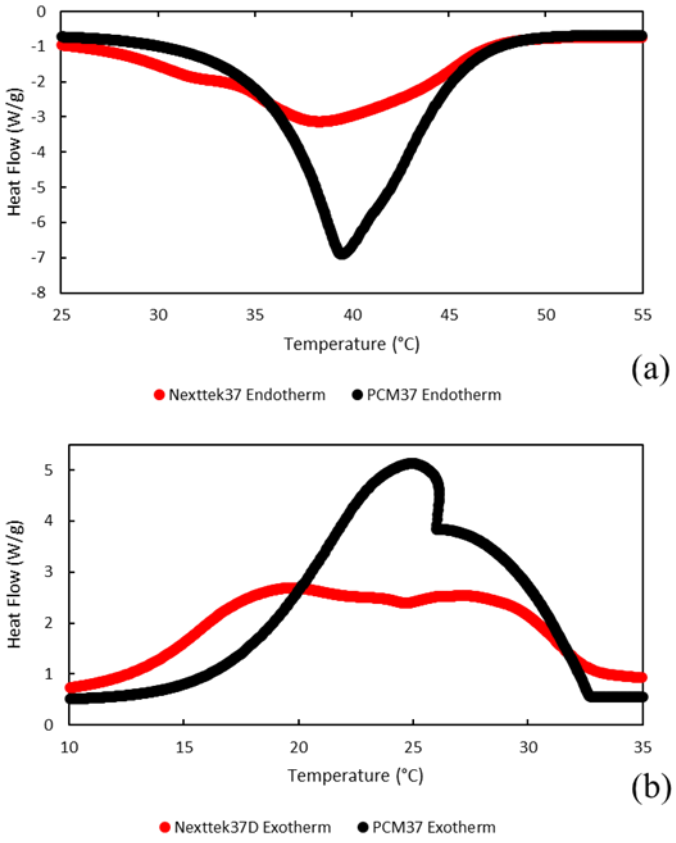

Figure 2.2.1: Endotherms (a) and Exotherms (b) of Nexttek37D and PCM37

The melting temperature of MPCM57D is advertised as 55°C – 59 °C on the SDS. The melting temperature of MPCM57D seen in Fig. 2.2.2(a) is 60.52°C. The onset temperature for MPCM57D melting in Fig. 2.2.2(a) is 48°C and the offset temperature is 70°C. The melting temperature of PCM57 in Fig. 2.2.2(a) is 61.05°C. The polymer shell on the MPCM57D does not play a large role in the enthalpy of fusion of PCM57D. The

onset temperature for PCM57 melting in Fig. 2.2.2(a) is 48°C and the offset temperature is 70°C. The solidification temperature of MPCM57D in Fig. 2.2.2(b) is 46.66°C. The onset temperature for MPCM57D solidification in Fig. 2.2.2(b) is 22°C and the offset is 60°C. The solidification temperature of the PCM57 seen in Fig. 2.2.2(b) is 50.41°C. The onset temperature for PCM57 solidification in Fig. 2.2.2(b) is 39°C and the offset temperature is 57°C.

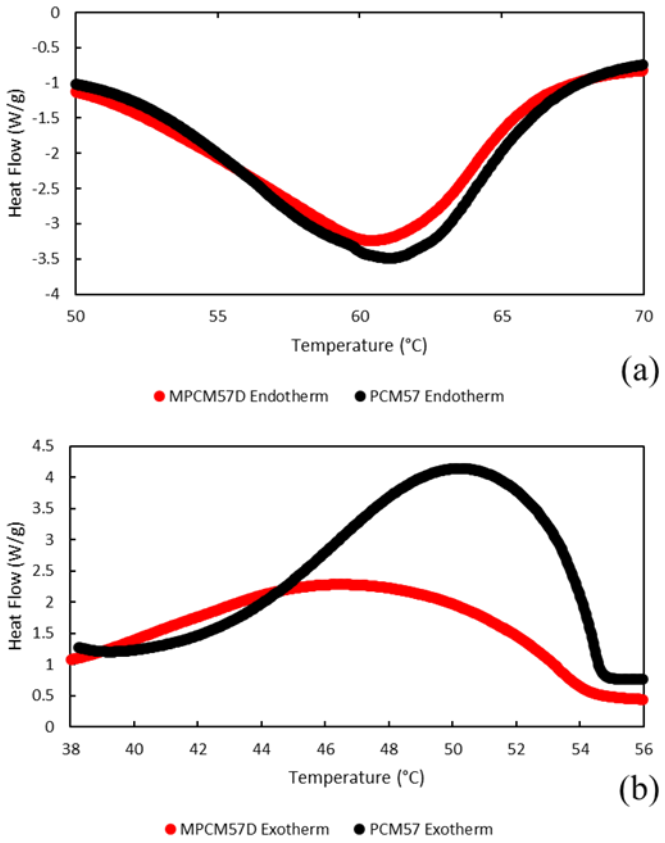

Figure 2.2.2: Endotherms (a) and Exotherms (b) of MPCM57D and PCM57

To better understand the impact of the encapsulation, the encapsulation ratio, R, of the MPCM which is defined by

$$R = \frac{\Delta H_{m,MPCM}}{\Delta H_{m,PCM}} \times 100\% \quad (1)$$

and is used to determine what concentration of the PCM was successfully encapsulated. The encapsulation efficiency, E, of the MPCM can be found by

$$E = \frac{\Delta H_{m,MPCM} + \Delta H_{s,MPCM}}{\Delta H_{m,PCM} + \Delta H_{s,PCM}} \times 100\% \quad (2)$$

to determine what the effectiveness of the MPCM latent heat responses. Table 2.2.1 shows enthalpies of PCM and encapsulated PCM which may be utilized to calculate the encapsulation ratio and efficiencies with experimental uncertainties shown in Table 2.2.2. Table 2.2.3 is reflective of the encapsulation efficiencies and encapsulation ratios of Nexttek37D and MPCM57D.

Table 2.2.1: Enthalpies of MPCMs and PCMs

Product	Enthalpy of Fusion (J/g)	Enthalpy of Crystalization (J/g)
Nexttek37D	178.9	170.1
PCM37	253.1	250.3
MPCM57D	133.4	144.2
PCM57	137.3	145.8

Table 2.2.2: Enthalpy uncertainty of MPCMs and PCMs.

± 95% Confidence Interval		
Product	Enthalpy of Melting (J/g)	Enthalpy of Solidification (J/g)
Nexttek37D	10.4	7.44
PCM37	2.74	7.84
MPCM57D	4.5	3.92
PCM57	8.23	1.37

Table 2.2.3: Encapsulation Ratio and Encapsulation Efficiencies of MPCMs

Product	Encapsulation Ratio, R	Encapsulation Efficiency, E
Nexttek37D	70.68%	69.33%
MPCM57D	97.16%	98.06%

2.3 TGA Procedure

The SDT Q600 is utilized to perform Thermogravimetric Analyzer (TGA). The weight change of the sample is measured over a temperature gradient. This machine is also capable of measuring heat flow as a Differential Scanning Calorimeter (DSC) would. Initially, the purge gas valves may be opened, the nitrogen gas is typically selected as the purge flow gas. Open the "TA Instrument Explorer" program. Select the "Q600-0671" in the window to launch the control software. Select Experiment View and access the Summary Page. Select "SDT Standard" from the mode list. Select "Custom" from the test list. Enter the sample name. Select the pan type, this will typically be alumina. Specify a data file name using the browse button. Click on the procedure page, enter method name, and click on the editor button. Create a method that controls the: sample interval, data storage, equilibrate, and ramp settings. Click on advanced settings to access advanced parameters and click on the "Post" to access post test parameters that allow you to specify furnace and air cool options. Click on the notes page, enter operator name, select "#1 Nitrogen" in mass flow control settings if that is the purge gas selected, and specify the flow rate as 100 $\frac{mL}{min}$. Click apply to ensure these changes are made. To begin the experiment, click on "Control", "Furnace", and "Open" to open the furnace. Obtain two clean 90 μL alumina pan and position them on the platforms that correspond with their size. Click "Control", then "Furnace", then "Close" to close the furnace. Once the mass on the right panel of the program stabilizes, click "Calibrate", then "Tare", and wait for stabilization of the mass. Open the furnace with the same procedure as previously described to do so. Remove the sample pan, the pan on the outside of the machine, from the platform and place 2-20 mg of the desired test material into the sample pan. Close the

furnace with the same procedure as previously described to do so. Click “Start the Run” button to begin the experiment. To transfer the data, click “Tools”, then “Data Transfer”, then retrieve the files in the selected export location. The data file can be interpreted and opened in TA Universal Analysis software. Wait till the furnace drops below 100°C, then open the furnace. Remove all samples from the furnace platforms and close the furnace. Close the control software and close the gas valve.

2.4 TGA Results

Thermogravimetric Analysis (TGA) testing was utilized to determine the thermal degradation properties of the PCM and MPCM. In Fig. 2.4.1(a), the Nexttek37D sample at 37°C the mass decreases at extremely small increments due to the density change of the new phase while maintaining the same density of the encapsulation polymer. The Nexttek37D encapsulation maintains its rigidity until a temperature of 300°C. At a temperature of 350°C, the weight of the Nexttek37D sample quickly declines, and during the experiment it was noted that evaporation of the material occurred. PCM37 does not begin to significantly lose weight percentage until 200°C in Fig. 2.4.1(a). In comparison to the Nexttek37D sample, there is no significant onset of a weight percentage decline at 200°C. Most of the weight percentage has thermally degraded at 290°C for PCM37. The MPCM57D encapsulation maintains its rigidity well until the temperature of 300°C in Fig. 2.4.1(b). At a temperature of 400°C, the weight of the MPCM57D sample quickly declines, and during the experiment it was noted that evaporation of the material occurred. In Fig. 2.4.1(b), the PCM57 does not begin to significantly lose weight until 200°C. In comparison to the MPCM57D sample, there is little to no significant onset of a

weight percentage decline at 200°C. Most of the weight percentage has thermally degraded at 350°C for PCM57.

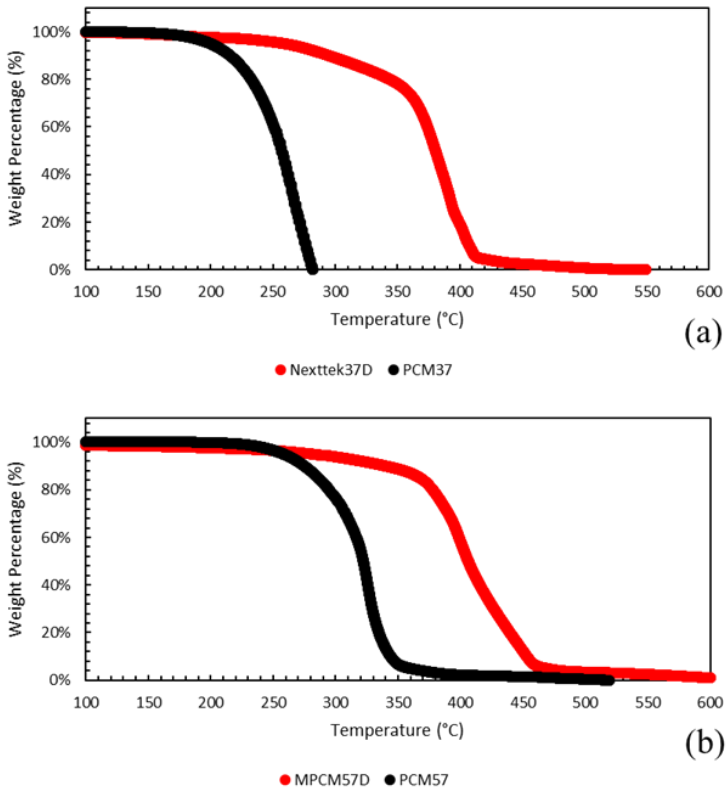

Figure 2.4.1: Thermal degradation of (a) Nexttek37D and PCM37, (b) MPCM57D and PCM57

2.5 Digital Microscope Procedure

To prepare the sample of Nexttek37D and MPCM57D to be observed under the microscope, collect 2 glass microscope slides to place the samples on. The MPCMs will not be observable without diluting the sample because they will naturally clump together. To dilute the sample, 10mL of isopropyl alcohol was mixed with > 1 mL of the desired MPCM sample and then mixed thoroughly by shaking the sample. A transfer pipet was

then used to place a couple droplets of the sample on the glass microscope slides. The isopropyl alcohol quickly evaporates, and you are left with observable results. Utilizing an Olympus BX51 WI, the samples were digitally examined.

To calibrate in ImageJ software, open the calibration slide digital scan for the desired objective. The calibration slide utilized has a length of 1mm. Draw a line on the calibration slide digital scan to prepare the calibration scale. In the ImageJ software, select the 'Analyze' tab and click 'Set Scale'. Enter the known distance and units and click 'OK'. To ensure this scale is used while analyzing scans of the same objective, check the 'Global' box, then click 'OK'. To measure distances in the software, draw a line/shape over the object you wish to analyze, and select the 'Analyze' tab, and select 'Measure'. Select the 'Edit' tab in the 'Measure' window that appears and hit 'Copy' to copy over results to the computer.

2.6 Digital Microscope Results

A digital microscope was utilized with ImageJ software to determine geometric dimensions of the MPCMs. Figures 2.6.1(a) and 2.6.2(a) show the paraffin wax core with a light blue coloration, and the shell with a white coloration. In Fig. 2.6.1(b) and Fig. 2.6.2(b), the digital microscope analyzes the range of MPCM diameters. The distribution of the MPCM diameters can be found in Fig. 2.6.3. The average diameter size of the Nexttek37D is 17.94 μm with a standard deviation of 4.52 μm. This yielded an average surface area of $1.01 \times 10^{-9}\ m^2$. If there is a cube of $5.78\ m^3$ filled with Nexttek37D, then the surface area of Nexttek37D within that cube would be $1.01 \times 10^{11}\ m^2$ or 25002863 acres. The average diameter size of the MPCM57D is 15.54 μm with a standard deviation of 6.41 μm. This yielded an average surface area of $7.59 \times 10^{-10}\ m^2$.

If there is a cube of 3.75 m^3 filled with MPCM57D, then the surface area of MPCM57D within that cube would be 75907880605 m^2 or 18757245 acres. MPCMs create a large surface area for whatever form they take. This vastly increases the heat transfer capabilities of a slurry. Figure 2.6.4 depicts the shell thickness distribution for the MPCMs. The average shell size of the Nexttek37D is 4.20 μm with a standard deviation of 1.361 μm. The average shell to diameter ratio is 0.234. The average shell size of the MPCM57D is 4.01 μm with a standard deviation of 1.509 μm.

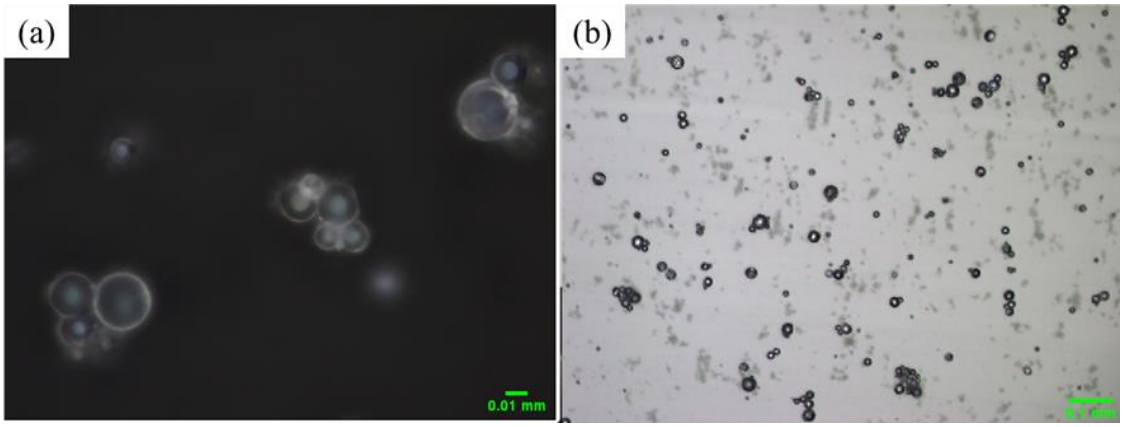

Figure 2.6.1: Digital microscope scans of (a) Nexttek37D at x50 magnification and (b) Nexttek37D at x10 magnification

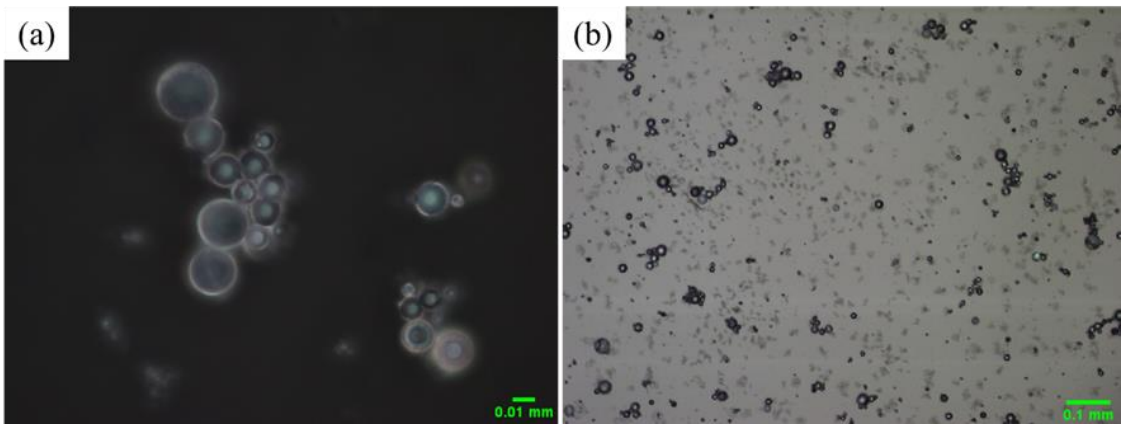

Figure 2.6.2: Digital microscope scans of (a) MPCM57D at x50 magnification and (b) MPCM57D at x10 magnification

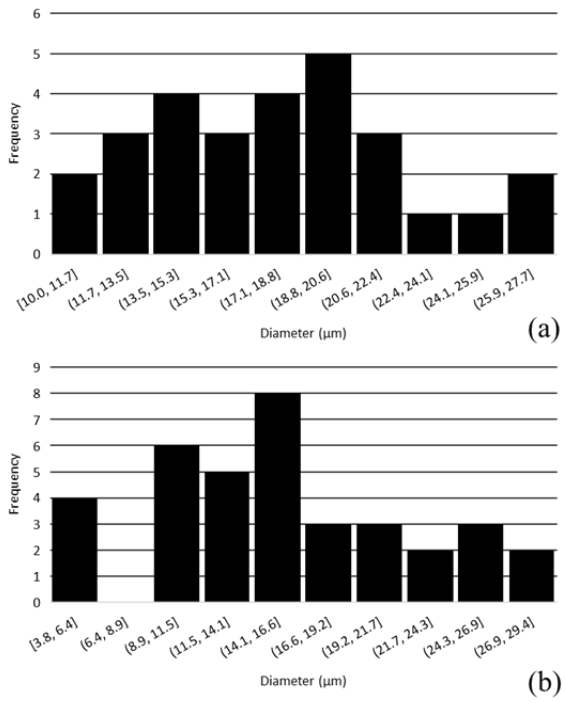

Figure 2.6.3: Diameter distributions of (a) Nexttek37D and (b) MPCM57D

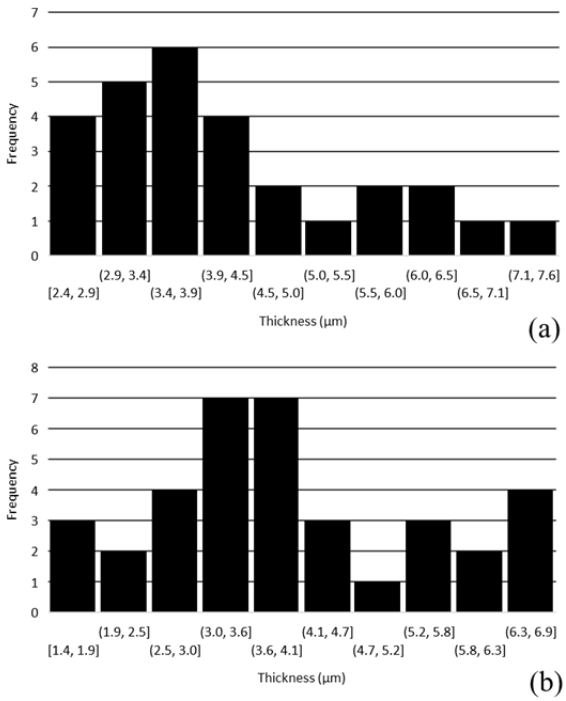

Figure 2.6.4: Thickness distributions of (a) Nexttek37D and (b) MPCM57D

The average shell to diameter ratio is 0.258. A reduced shell size can maximize the latent heat capacity of each MPCM; therefore, Nexttek37D stores more paraffin wax per unit volume.

Chapter III. MPCM Water Slurry Characterization

Utilizing the dynamic viscosity of slurry defined by [29]

$$\mu_{slurry} = \mu_w(1 - \alpha - 1.16\alpha^2)^{-2.5} \tag{3}$$

The effect of the MPCM concentration on the dynamic viscosity of the slurries can be found as shown in Table 3.1 It should be noticed that the calculation is based on a temperature of 20°C . As shown, when the MPCM concentration increases, the dynamic viscosity goes up. The density of the slurry depends on the MPCM concentration which can be predicted by [29],

$$\rho_{slurry} = (1 - \phi)\rho_w + \phi\rho_{MPCM} \tag{4}$$

As shown in Table 3.2, the density of the slurry decreases as the MPCM concentration increases. The effective thermal conductivity of the MPCM slurry can be estimated by [30],

$$k_{slurry} = k_w \frac{2+\frac{k_{MPCM}}{k_w}+2\alpha(\frac{k_{MPCM}}{k_w}-1)}{2+\frac{k_{MPCM}}{k_w}-2\alpha(\frac{k_{MPCM}}{k_w}-1)} \tag{5}$$

The thermal conductivities of the slurry concentrations can be seen in Table 3.3. There is little change in the thermal conductivity from water to the MPCM water slurry. The effective specific heat can be calculated by [30],

$$C_{p,slurry} = (1 - \phi)C_{p,w} + \phi C_{p,MPCM} \tag{6}$$

where the specific heat of the MPCM which can be calculated by [30],

$$C_{p,MPCM} = C_{p,PCM} + \left\{\frac{\pi}{2}\left(\frac{\Delta H_{m,PCM}}{T_{MR}} - C_{p,PCM}\right)\sin(\pi)\left[\frac{T-T_o}{T_{MR}}\right]\right\} \quad (7)$$

From Fig. 3.1, it can be found that the specific heat depends on temperature.

Table 3.1: The MPCM at different concentrations Dynamic Viscosities

Nexttek37D		
MPCM Weight Percentage (%)	MPCM Volume Percentage (%)	Dynamic Viscosity (N • s/ m^2)
1.0%	2.6%	0.00107
2.0%	5.3%	0.00116
3.0%	8.1%	0.00126
4.0%	10.9%	0.00138
5.0%	13.7%	0.00153
MPCM57D		
MPCM Weight Percentage (%)	MPCM Volume Percentage (%)	Dynamic Viscosity (N • s/ m^2)
1.0%	2.0%	0.00105
2.0%	4.0%	0.00111
3.0%	6.1%	0.00118
4.0%	8.2%	0.00126
5.0%	10.4%	0.00136

Table 3.2: The Density of the MPCMs at 20°C

	Density (kg/m^3)
Water	999.00
MPCM57D	508.24
Nexttek37D	383.33
Slurry	
1% MPCM57D	994.09
2% MPCM57D	989.18
3% MPCM57D	984.28
4% MPCM57D	925.98
5% MPCM57D	921.63
1% Nexttek37D	992.84
2% Nexttek37D	986.69
3% Nexttek37D	980.53
4% Nexttek37D	974.37
5% Nexttek37D	968.22

Table 3.3: The Thermal Conductivities of the MPCMs at 20°C

Thermal Conducitivty (W/m*K)		
Nexttek37D	MPCM57D	Water
0.394379673	0.42	0.60
Mass Percentage	Nexttek37D (W/m*K)	MPCM57D (W/m*K)
1.00%	0.60	0.60
2.00%	0.59	0.59
3.00%	0.58	0.59
4.00%	0.58	0.59
5.00%	0.57	0.58

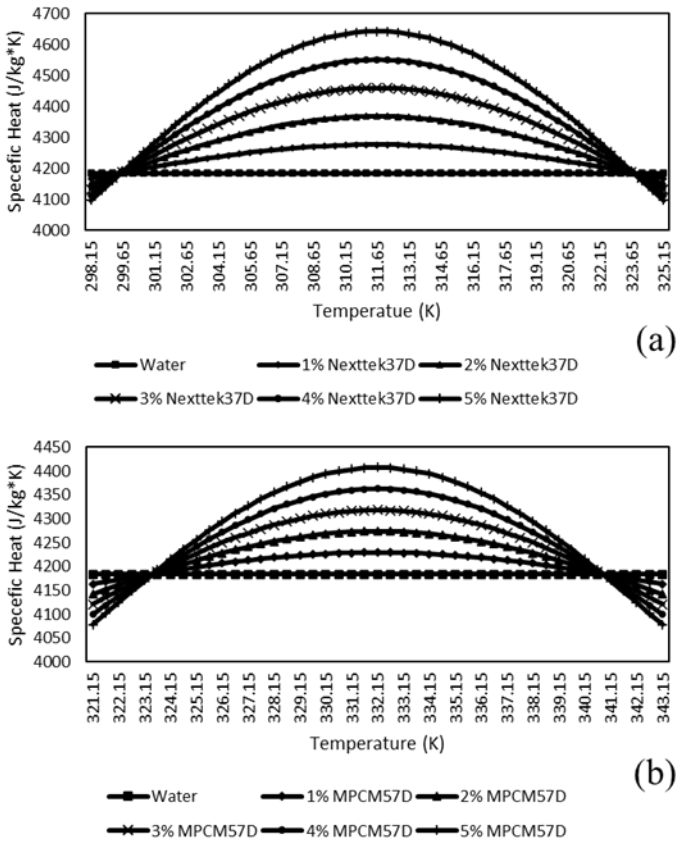

Figure 3.1: Specific Heat distributions of (a) Nexttek37D and (b) MPCM57D at 20°C

Chapter IV. Experimental Investigation

4.1 Experimental Setup

The schematic drawing of the experimental setup is shown in Fig. 4.1.1. The actual set up of the experiment is shown in Fig. 4.1.2. The setup consists of a copper OHP, an evaporating block, cartridge heaters, a DC power supply, a condensing block, a cooling bath, silicone tubing, hose clamps, a vacuum, a cold trap, a pressure transducer, insulation material, a data acquisition system, thermocouples, a computer, and data analysis software. The DC power supply is connected to the cartridge heaters and supplies the power input to the OHP. The power was calculated utilizing,

$$P = IV \tag{8}$$

The condensing is made from a 115 × 38 mm^2 aluminum block and is connected to a cooling bath line that pumps water at a constant temperature of 20°C or 40°C dependent upon the experiment. For experimental iteration 1, a cooling bath temperature of 20°C was utilized. When Nexttek37D was serving as the particulate in the slurry for experimental iteration 2 the cooling bath temperature is 20°C. When MPCM57D was serving as the particulate in the slurry for experimental iteration 2 the cooling bath temperature is 40°C. The evaporator is made from a 63 × 33 mm^2 aluminum block machined to fit four cartridge heaters with a maximum heat output of 600 W. The evaporating block, condensing block, a thin silicon sheet, a plastic outer ring, and insulation materials are fastened around the OHP with butterfly nuts and a screw. A thin film of OMEGATHERM-201 silicone grease is applied between surfaces to minimize heat loss of the system. As seen in the detailed drawing in Fig 4.1.3, the OHP total length is 107 mm, with an evaporation section length of 28 mm, an adiabatic section length of

42 mm, and a condensation section length of 37 mm. The complete OHP assembly is comprised of a copper base with a machined 3 × 3 mm^2 square cross-section channel which is bolted to a transparent polycarbonate cover plate, with a 0.5 mm thick high-temperature resistant silicone sheet lying between. Insulation material covers the entire OHP to prevent heat loss to the outside environment. The OHP is evacuated before it is charged by a Vacuubrand RZ-9 vacuum pump. The OHP is then charged to a 50% fill ratio with varying concentrations of MPCMs in water slurry. The 50% fill ratio holds a volume of 5.6 mL within the OHP. The MPCMs concentrations by weight fractions for experimental iteration 1 are 0%, .33%, .66%, and 1%. The MPCMs concentrations by weight fractions for experimental iteration 2 are 0%, 1%, 2%, 3%, 4%, and 5%. There are two types of MPCMs from Microtek Laboratories, Inc. to be tested: Nexttek37D and MPCM57D. Table 4.1.1 and Table 4.1.2 show the mass of the MPCMs and deionized water in the prepared samples which are increasingly opaque as the weight concentration increases.

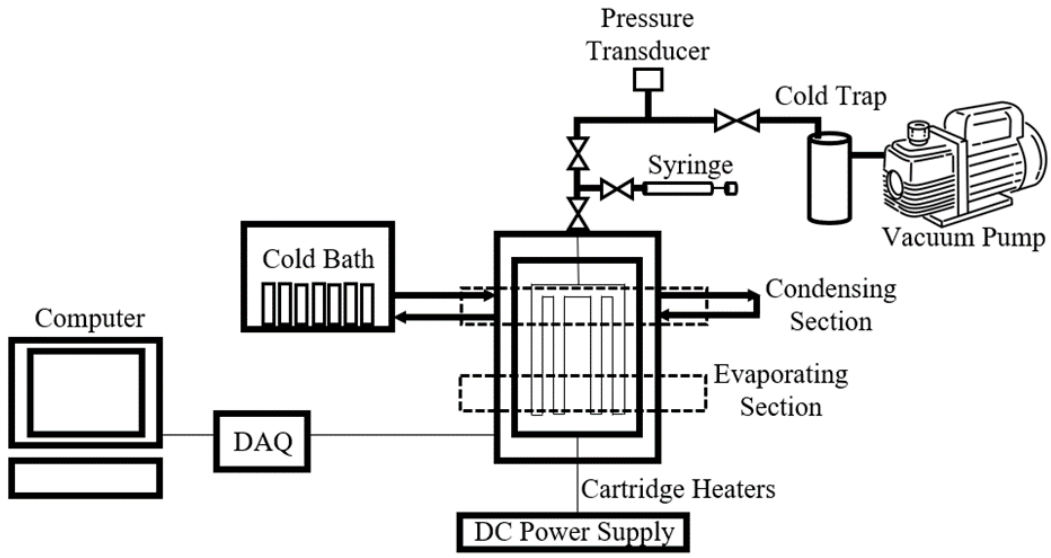

Figure 4.1.1: Schematic of the experimental setup

Figure 4.1.2: Photo of the experimental setup

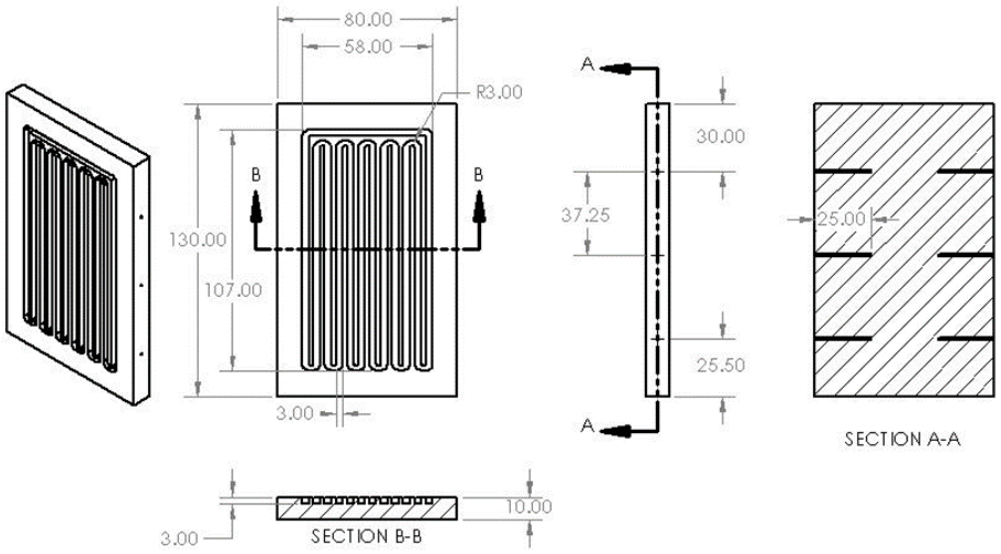

Figure 4.1.3: Dimensions of OHP with thermocouple ports (all dimensions are in mm)

Table 4.1.1: Sample sizes of Nexttek37D at 50% fill ratio

Nexttek37D			
Total Weight (g)	Water Weight (g)	PCM Weight Percentage (%)	PCM Weight (g)
273.03	272.13	0.33%	0.90
69.70	69.24	0.66%	0.46
92.01	91.09	1.00%	0.92
100.00	98.00	2.00%	2.00
85.97	83.39	3.00%	2.58
100.00	96.00	4.00%	4.00
65.26	62.00	5.00%	3.26

Table 4.1.2: Sample sizes of MPCM57D at 50% fill ratio

MPCM57D			
Total Weight (g)	Water Weight (g)	PCM Weight Percentage (%)	PCM Weight (g)
223.94	223.20	0.33%	0.74
115.15	114.39	0.66%	0.76
172.00	170.28	1.00%	1.72
100.00	98.00	2.00%	2.00
83.97	81.45	3.00%	2.52
100.00	96.00	4.00%	4.00
75.34	71.57	5.00%	3.77

Eight T-type thermocouples are implemented into the system to track the temperature. Six thermocouples are inserted into the OHP as seen in Fig. 4.1.3 thermocouple holes to measure the temperature variations: two in the condensing section, two in the adiabatic

section, and two in the evaporating section. The remaining two thermocouples are inserted into the inlet and outlet of the condenser block. The temperature data for experimental iteration 1 is collected by a Measurement Computing USB-2408 and DAQami software. The temperature data for experimental iteration 2 is collected by a Keithley 2701 and Keithley Kickstart software. The heating input varies from 100 W to 400 W in 100 W increments. The differing power increments were adjusted by changing voltage and amperage as seen in Table 4.1.3. The thermal conductance of the OHP is calculated by

$$C = \frac{Q_e}{\bar{T}_e - \bar{T}_c} \tag{9}$$

Table 4.1.3: Differing power inputs for the experiment

Voltage (V)	Current (A)	Power (W)
49.00	2.04	100.01
69.30	2.89	200.00
85.40	3.51	300.01
98.50	4.06	400.01

4.2 Experimental Procedure

4.2.1 Backfill Process

While there is no working fluid in the OHP, close the filling channel using forceps, and open the forceps connected to the Vacuubrand RZ-9 vacuum pump channel. Turn the vacuum pump on and ensure the valves across the top of the line between the OHP and vacuum pump are open. Ensure a vacuum is achieved using the MKS vacuum pressure transducer with a minimum reading of at least ~20 torr (1 atm = 760 torr). Close the forceps connected to the line that connect the OHP to the vacuum pump, and immediately open the forceps connected to the charging line, which is prepared with

~11.2 g of deionized (DI) water to ensure a 100% fill of the OHP. This will completely fill the OHP with the DI water. Once the water has flooded the OHP, close the clamp to the charging tube. Turn on the Agilent Technologies N5750A DC Power Supply and apply a power of at least 100 W. Ensure the DAQami or Keithley Kickstart software collects temperature data. Once the internal temperature of the evaporator section reaches 60°C, the vacuum is turned on and the forceps connected to the vacuum line are opened. This will cause the DI water to rapidly evaporate out of the OHP, ensuring no non-condensable gas (air) is in the system. Turn on the cooling baths recirculation feature to bring the temperature of the system to the desirable starting temperature. Periodically drain the cold trap to ensure there is not leaking into vacuum.

4.2.2 Charging Process

Prepare a sample of interest and fill it into a syringe to 5.6 mL or an equivalent 50% fill ratio for the OHP system. Before connecting the syringe to the charging line, ensure there are no bubbles or air trapped in the syringe. Ensure the charging line is closed with forceps and connect the syringe to the end of the charging line. Once the evaporating section reaches a temperature less than 40°C, open the charging line forceps while ensuring the line to the vacuum is closed. If the working fluid does not rapidly fill the OHP, then the vacuum of the OHP is not satisfactory.

4.2.3 Data Collection Process

Before collecting data, ensure the thermocouples reach a temperature of roughly 20°C or 40°C depending on the test performed. Eight T-type thermocouples are implemented into the system to track the temperature. Ensure the eight thermocouples are appropriately named, configured, and aligned with the proper channel in the DAQami or

Keithley Kickstart software. The heating input varies from 100 W to 400 W with 100 W increments. With 5 minutes of transient response before a steady state system is achieved at each discrete power level.

4.3 System Heat Loss Analysis

The heat input was added to the evaporating section by cartridge heaters. The power input into the heater can be readily determined by measuring the current and voltage. Although the insulation has been used, the heat loss still exists. To determine the heat loss, an experimental investigation of the energy balance measurement was conducted. If there is no heat loss, the heat added on the evaporator section should be equal to the thermal energy removed from the condenser by the coolant. The heat removed from the OHP condenser can be determined by

$$Q = C_p \dot{m}(T_{out} - T_{in}) \tag{10}$$

where C_p is the coolant heat capacity, T_{in} is the coolant inlet temperature, T_{out} is the coolant outlet temperature, and $\dot{m}$ is the coolant flow rate. This heat transfer rate from the condenser was then compared to the input heat rate to determine the heat loss of the system. The mass flow rate of the system was found as 21 $\frac{mL}{s}$. The specific heat of water at 20°C is 4184 $\frac{J}{kg \times K}$. The temperature difference was allowed to reach equilibrium at each power step from 100 W to 400 W in 100 W increments as seen in Fig. 4.3.1. The heat loss out of the system is a maximum of 6.85% at 300 W and a minimum of 2.79% at 100 W as seen in Fig. 4.3.2.

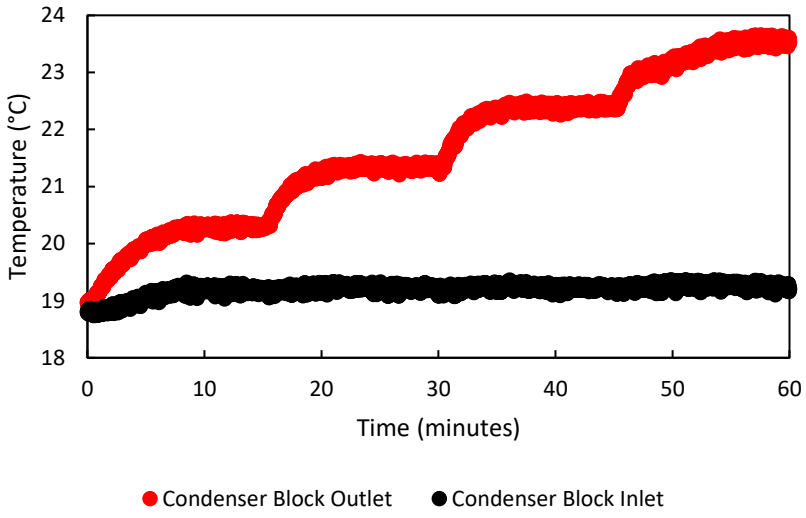

Figure 4.3.1: Condenser Inlet and Outlet temperature response at 100 W to 400 W in 100 W increments for 15 minutes

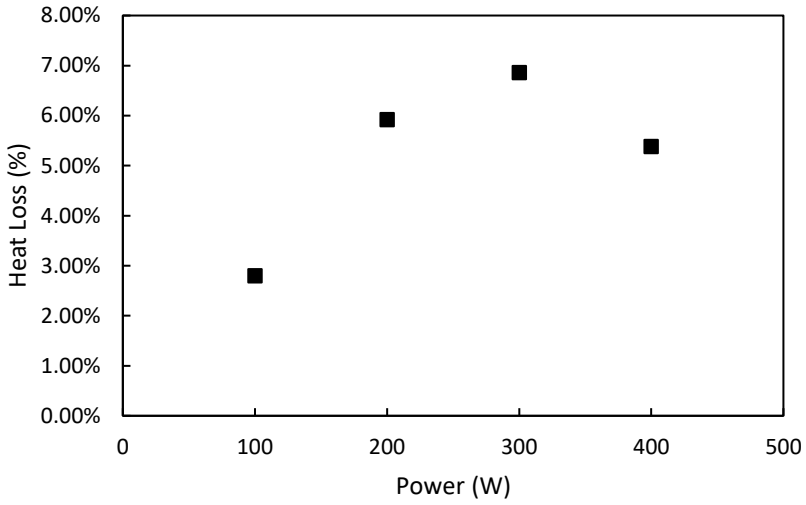

Figure 4.3.2: Heat loss of the OHP system at 100 W to 400 W in 100 W increments

4.4 Iteration 1 Experimental Results

The OHP charged with weight fractions of 0.33%, 0.66%, and 1% of MPCM was tested. The OHP was able to start up at a minimum heat input of 100 W when charged with DI water and the various weight fractions of MPCM. Prior to startup, small vapor bubbles

began to form at the walls of the evaporator section of the OHP. The vapor bubbles then grew larger and began to detach from the wall, coalescing together. A stream of small vapor bubbles would rise from the evaporator section with increasing frequency and begin to grow until distinct vapor plugs and liquid slugs were formed, and oscillation began. No dry out was observed at each power level. Figures 4.4.1, 4.4.2 and 4.4.3 show the transient temperature response across the OHP when charged with DI water, Nexttek37D, and MPCM57D respectively. At each power input, the temperature of all three sections of the OHP underwent a steep initial rise before eventually reaching a steady state response. Achieving an isothermal temperature for the condenser inlet and outlet was not done throughout the experiment because the temperature rises slowly in the condenser inlet and outlet. Although, this has little impact on analysis of the experiment. While Figs. 4.4.1-4.4.3 provide important data for the experiment, there are not visually distinguishable results from these plots.

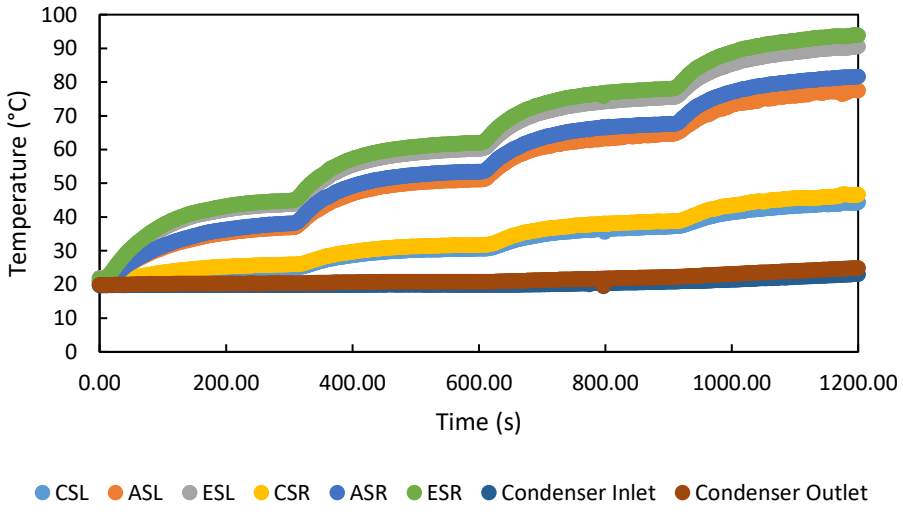

Figure 4.4.1: The temperature distribution for the experiment for DI water

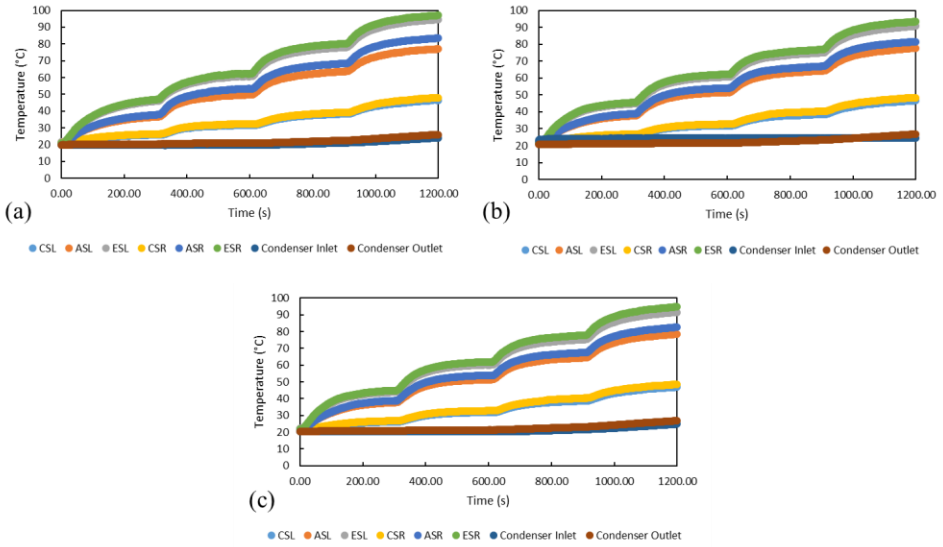

Figure 4.4.2: The temperature distribution for the experiment for differing Nexttek37D concentrations a) 0.33%, b) 0.66%, and c) 1%

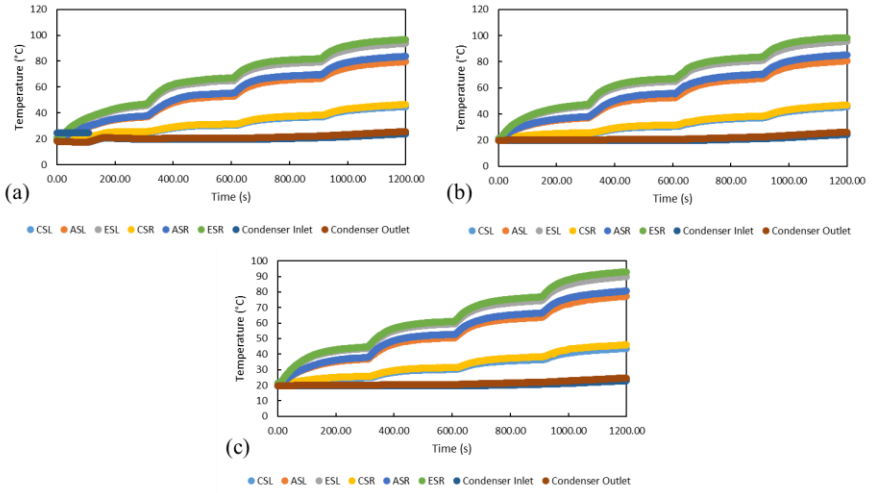

Figure 4.4.3: The temperature distribution for the experiment for differing MPCM57D concentrations a) 0.33%, b) 0.66%, and c) 1%

The starting temperatures around 20-22°C never reached above 100°C for the performed experiments. Additionally, the right side of the evaporating section is seen noticeably larger than that of the left side of the evaporating sections because the condenser inlet is fixed on the left side. The condensate quickly absorbs sensible heat on

the left side of the condenser and transfers less heat on the right side of the evaporator block due to a smaller temperature difference as seen in Eq. (10).

Figures 4.4.5 and 4.4.6 show the temperature response of the OHP above the melting temperatures of Nexttek37D and MPCM57D, which are 37°C and 57°C respectively. This result shows that increasing the weight fraction of MPCM lowered the rise in temperature of the evaporator section of the OHP for both MPCM brands tested. However, using pure water provided the lowest evaporator temperature above the melting temperature values of each MPCMs. The MPCMs microfluid thermal transport is decreased before the melting temperature of the MPCMs but increases temporarily when the melting range temperature is reached. In Fig. 4.4.5, the Nexttek37D is exposed to the applied power of 100 W for longer than that of water but leaves the plot at the same temperature difference. In Fig. 4.4.5, if tangent lines were drawn for slopes of each line at 130 seconds, the 1% Nexttek37D concentration would have a smaller slope than that of water. In Fig. 4.4.6 there is little distinguishability between 0.33% and 0.66% MPCM57D. Figure 4.4.6 shows that water reaches a temperature of 57°C before the MPCM57D microfluids. Additionally, in Fig. 4.4.6, the 1% MPCM57D appears to achieve a steady state temperature before that of water, although the steady state temperature is larger than that of water.

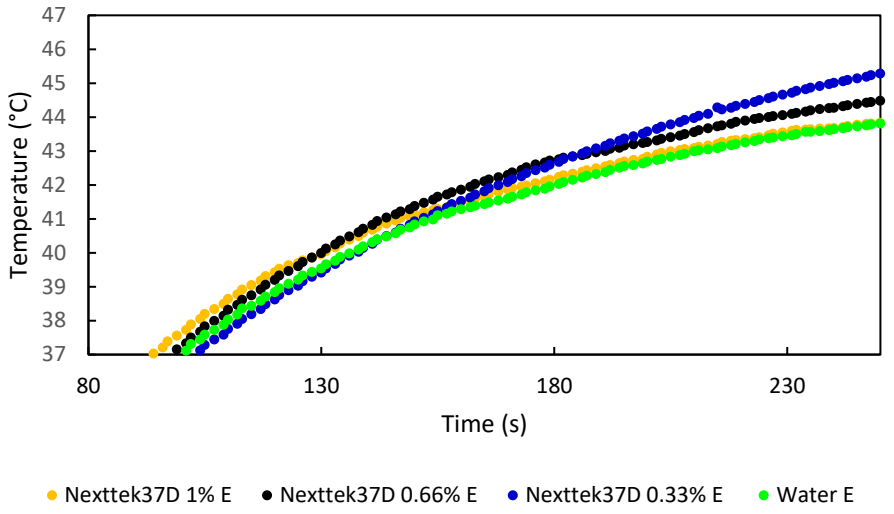

Figure 4.4.5: The melting range data for evaporator temperature for differing Nexttek37D microfluid concentrations

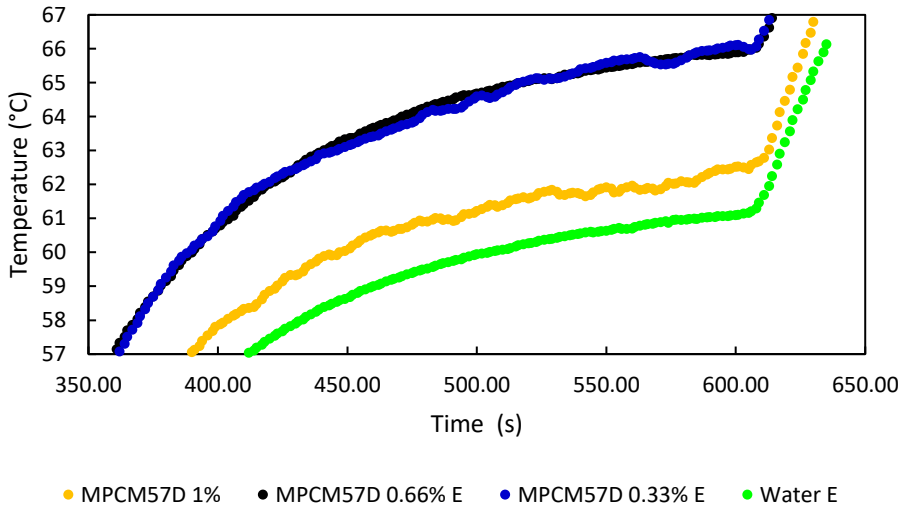

Figure 4.4.6: The melting range data for evaporator temperature for differing MPCM57D microfluid concentrations

Figures 4.4.7 and 4.4.8 show the results of the OHP's thermal conductance when charged with water and the microfluids with various weight fractions of MPCM. As the power input increased, the thermal conductance of the OHP increased in an approximately linear trend for all the working fluids tested. In Fig. 4.4.7, both Nexttek37D concentrations of

0.66% and 1% outperformed water at power inputs of 200 W and above. 1% Nexttek37D was far superior with a thermal conductance increase of 3.68% to the thermal conductance of water at 200 W. At 400W, the 0.66% weight fraction Nexttek37D working fluid achieved the highest thermal conductance of 8.75 $\frac{W}{K}$. In Fig. 4.4.8, water always had the largest thermal conductance followed by the 1% MPCM57D for each trial. In Fig. 4.4.8, the deviation between MPM57D and water gets smaller as power increases. A possible explanation for this phenomenon is superheated melting because the PCM melts above its natural melting temperature due to the low thermal conductance of the microencapsulation shell.

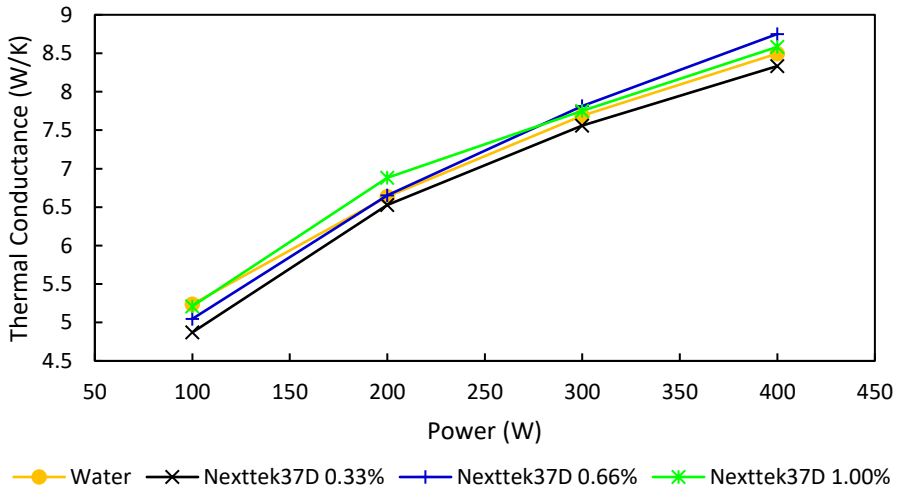

Figure 4.4.7: Thermal conductance for differing Nexttek37D microfluid concentrations over varying heat inputs

Table 4.4.1: The uncertainty of the thermal conductance for the Nexttek37D slurry in iteration 1

	Nexttek37D Thermal Coductance 95% Confidence Interval (W/K)			
Weight Percent MPCM (%) / Power Level (W)	100	200	300	400
0%	0.13	0.07	0.07	0.12
0.33%	0.10	0.53	0.22	0.25
0.66%	0.62	0.40	0.76	0.46
1%	0.77	0.29	0.70	0.45

Table 4.4.1 and Table 4.4.2 show some of the dataset have large uncertainties.

MPCM57D 0.33% has an uncertainty of +/- 1.04 $\frac{W}{K}$.

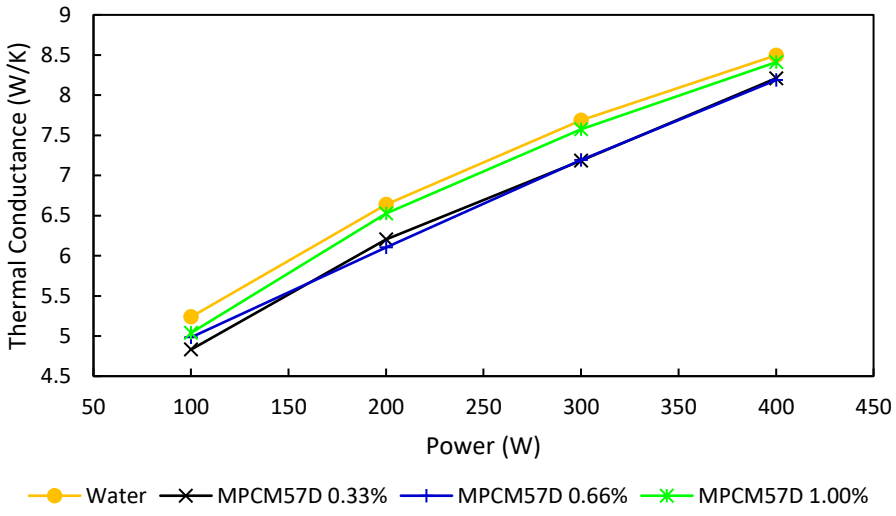

Figure 4.4.8: Thermal conductance for differing MPCM57D microfluid concentrations over varying heat inputs

Table 4.4.2: The uncertainty of the thermal conductance for the MPCM57D slurry in iteration 1

	MPCM57D Thermal Coductance 95% Confidence Interval (W/K)			
Weight Percent MPCM (%) / Power Level (W)	100	200	300	400
0%	0.13	0.07	0.07	0.12
0.33%	0.02	1.04	0.42	0.28
0.66%	0.56	0.75	0.87	0.63
1%	0.50	0.50	0.49	0.32

To calculate experimental effective thermal conductivity of a OHP Eq. (11) can be utilized,

$$k_{eff,OHP} = \frac{QL_{eff}}{A_c \Delta T} \quad (11)$$

The thermal conductivity of copper is found as 400 $\frac{W}{m \times K}$. Table 4.4.1 provides the experimental effective thermal conductivities.

Table 4.4.3: The experimental effective thermal conductivity of the OHP with differing power inputs and working fluids

Working Fluid Slurry	Water	Nexttek37D			MPCM57D		
Concentration (%)	100	0.33	0.66	1	0.33	0.66	1
Power (W)	Thermal Conductivity (W/m*K)						
100	425.5	395.7	408.4	421.0	392.5	403.6	408.3
200	539.2	529.4	539.9	558.9	500.3	494.1	529.6
300	624.6	613.9	633.3	628.5	583.2	582.2	614.9
400	690.3	676.9	710.5	696.9	666.9	664.2	683.1

The experimental effective thermal conductivity is seen to improve the thermal conductivity as compared to copper across all but the 0.33% MPCM microfluids. These results are parallel to that of the thermal conductance in terms of the patterns displayed. Although, comparing this value to the thermal conductivity of copper offers good context to the efficiency of the OHP. As the input power increases, the effective thermal conductivity and heat transport capabilities improve as well.

4.5 Iteration 1 Conclusion

An experimental investigation of an oscillating heat pipe utilizing a working fluid of MPCM suspended in water was conducted to study the effects on its heat transfer performance. Two types of Microtek MPCMs, Nexttek37D and MPCM57D, were tested in weight fractions of 0.33%, 0.66%, and 1%. Startup and oscillation of the working fluid in the OHP was still achieved with the implementation of MPCMs. For both types of MPCM, increasing the weight fraction of MPCM reduced the rise of temperature of the evaporating section of the OHP around their phase-change temperature. Across 200-400

W power inputs, using 0.66% and 1% Nexttek37D mass concentrations as the working fluid achieved a similar or greater thermal conductance as compared to using pure water. However, across all heat inputs, using a MPCM57D enhanced working fluid achieved a similar or lesser thermal conductance as compared to using pure water. The 0.66% weight concentration of Nexttek37D was found to perform the best, achieving a thermal conductance of 8.75 $\frac{W}{K}$ at 400 W, a 3.68% increase in heat transfer performance over using pure water.

4.6 Iteration 2 Experimental Results

The OHP charged with weight fractions of 1%, 2%, 3%, 4%, and 5% of Nexttek37D and MPCM57D were tested. The OHP began oscillations at a minimum heat input of 100W. Dry out did not occur for each of the discrete power levels. At each power input, the temperature of all three sections of the OHP underwent a steep initial rise before eventually reaching a steady state response. The condensing bath temperature remained constant throughout the experiment as the mass flow rate was increased till an isothermal response was achieved. The temperature response of the thermocouples can be seen in Fig. 4.6.1(a) for condensing bath temperature of 20°C and Fig. 4.6.1(b) for condensing bath temperature of 40°C. The temperature of the Nexttek37D slurry experiments never reached above 100°C. The temperature of the MPCM57D slurry experiments never reached above 110°C.

The MPCM slurries thermal transport is decreased before the melting temperature of the MPCMs but increases temporarily when the melting range temperature is reached. In Fig. 4.6.2(a), the water temperature response in the evaporating section of the OHP during the melting temperature range of Nexttek37D climbs at a faster rate than the

Nexttek37D slurry. During the time span in Fig. 4.6.2(a), the lowest temperature of the evaporator can be found in the 3% Nexttek37D and 4% Nexttek37D slurries. In Fig. 4.6.2(b), MPCM57D has the smallest temperature change and water has the largest temperature change in the time span seen in the plot. This data agrees with Fig 3.1(b) which shows 5% MPCM57D will have the largest specific heat in the melting temperature range.

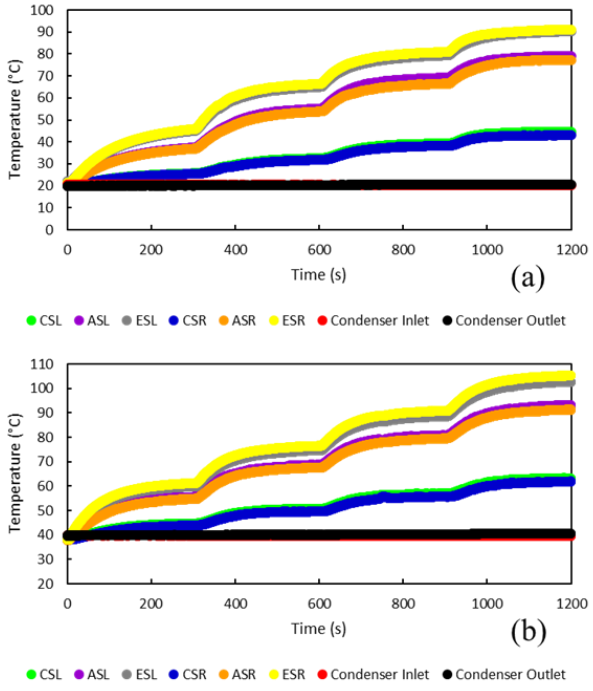

Figure 4.6.1: The temperature response of the thermocouples (a) for Nexttek37D slurry and (b) for MPCM57D slurry

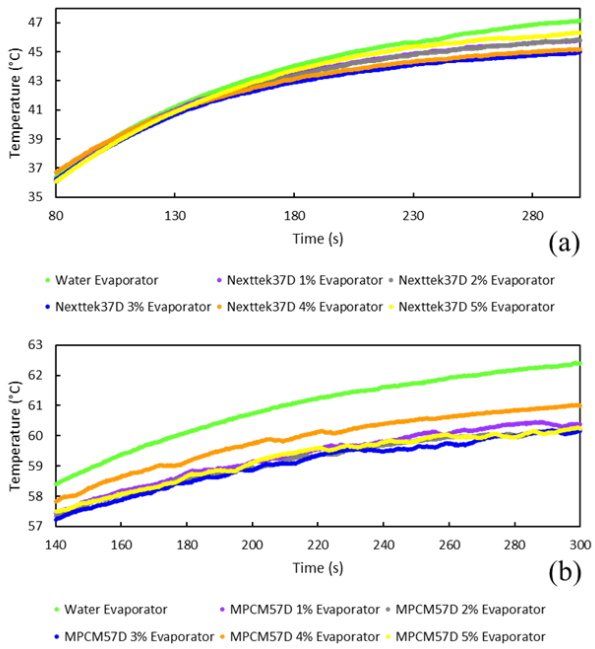

Figure 4.6.2: The temperature response in the melting temperature ranges for the thermocouples (a) of Nexttek37D slurry and (b) of MPCM57D slurry

The thermal conductance of the OHP is enhanced with Nexttek37D slurry working fluid at all concentrations and powers except for 5% Nexttek37D at 300 W and 400 W as seen in Fig. 4.6.3(a). Nexttek37D at weight concentrations of 1%, 2% and 4% perform similarly at all power levels. 3% Nexttek37D performs the best comparatively to the other Nexttek37D concentrations. The thermal conductance of the OHP is enhanced with MPCM57D slurry working fluid at all concentrations and powers as seen in Fig. 4.6.3(b).

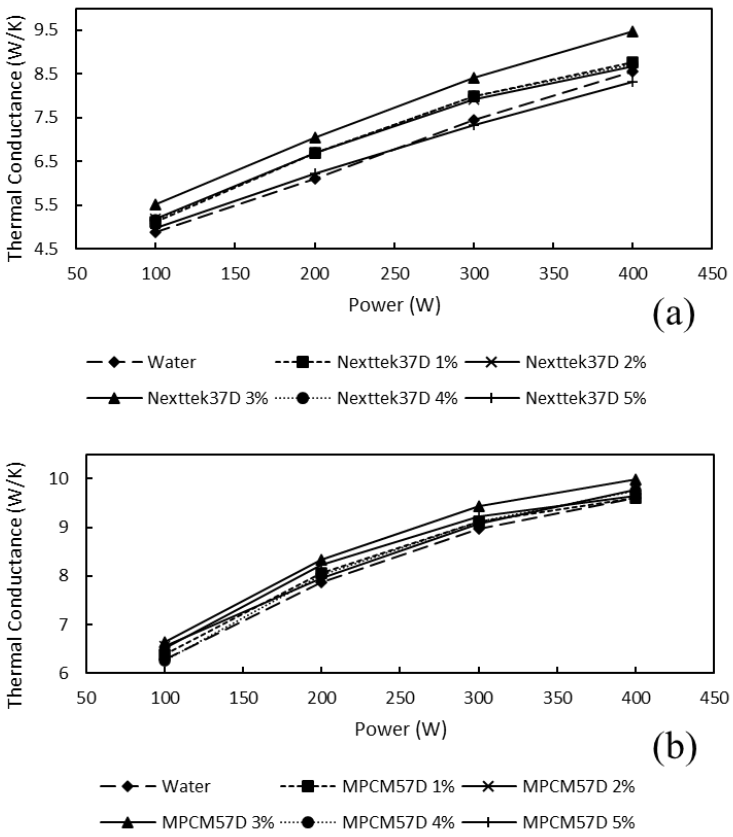

Figure 4.6.3: The thermal conductance at discrete power levels (a) of Nexttek37D slurry and (b) of MPCM57D slurry

A MPCM57D concentration of 3% performed the best out of all MPCM57D weight concentrations tested. Nexttek37D at 200W and a concentration of 3% serves a 15.499% improvement over that of water as seen in Table 4.6.1. The Nexttek37D slurries perform the best at a 200W power input. Additionally, the thermal conductance is enhanced as power input increases. MPCM57D at 200W and a concentration of 3% serves a 5.806% improvement over that of water as seen in Table 4.6.3. Table 4.6.2 and Table 4.6.4 quantify the 95% confidence interval for the thermal conductance calculated. The statistical uncertainties experienced in the experiment for Nexttek37D and MPCM57D are small and reflect accurate data collection.

Table 4.6.1: The Thermal Conductance percent change compared to water for Nexttek37D

	Thermal Conductance Percent Change Compared to Water				
Power (W)	Nexttek37D 1%	Nexttek37D 2%	Nexttek37D 3%	Nexttek37D 4%	Nexttek37D 5%
100	4.9%	6.1%	13.1%	5.7%	1.7%
200	9.7%	9.7%	15.5%	9.9%	1.8%
300	7.2%	6.3%	13.0%	7.2%	-1.7%
400	2.5%	1.4%	10.8%	1.9%	-2.6%

Table 4.6.2: The uncertainty of the thermal conductance for the Nexttek37D slurry in iteration 2

	Nexttek37D Thermal Coductance 95% Confidence Interval (W/K)			
Weight Percent MPCM (%) / Power Level (W)	100	200	300	400
0%	0.31	0.26	0.40	0.07
1%	0.15	0.06	0.05	0.03
2%	0.23	0.07	0.08	0.17
3%	0.27	0.15	0.10	0.16
4%	0.25	0.34	0.39	0.38
5%	0.07	0.22	0.17	0.12

Table 4.6.3: The Thermal Conductance percent change compared to water for MPCM57D

	Thermal Conductance Percent Change Compared to Water				
Power (W)	MPCM57D 1%	MPCM57D 2%	MPCM57D 3%	MPCM57D 4%	MPCM57D 5%
100	1.4%	4.3%	5.7%	-0.6%	3.5%
200	2.5%	1.1%	5.8%	1.9%	4.5%
300	1.7%	1.4%	5.3%	1.9%	3.1%
400	0.0%	1.6%	3.8%	1.5%	0.4%

Table 4.6.4: The uncertainty of the thermal conductance for the MPCM57D slurry in iteration 2

	MPCM57D Thermal Coductance 95% Confidence Interval (W/K)			
Weight Percent MPCM (%) / Power Level (W)	100	200	300	400
0%	0.254	0.02	0.09	0.04
1%	0.195	0.06	0.09	0.16
2%	0.00392	0.14	0.07	0.12
3%	0.0568	0.13	0.06	0.14
4%	0.0313	0.20	0.24	0.19
5%	0.164	0.04	0.06	0.19

4.7 Iteration 2 Conclusion

An experimental investigation was carried out to determine the heat transport capabilities of an OHP with an MPCM slurry working fluid at weight concentrations 0-5%. To produce peak heat transport, temperature ranges for the testing environments were selected around the PCM melting temperature range. A recirculating cooling bath

temperature for Nexttek37D slurries was selected at 20°C because the experimental melting temperature of Nexttek37D is 39.47°C. Additionally, recirculating cooling bath temperature for MPCM57D slurries was selected at 40°C because the experimental melting temperature of MPCM57D is 60.52°C. OHP performance was optimally enhanced when the MPCM were at a weight concentration of 3% in the slurry. For the MPCM57D slurries, the average improvement of thermal conductance as compared to water across all power levels is 5.14%. For the Nexttek37D slurries, the average improvement of thermal conductance as compared to water across all power levels com is 13.09%. Most MPCM in water slurries yielded improvement over water working fluid in the OHP. The MPCM slurries generated the best results at a power level of 200W. As the discrete power level increased, thermal conductance also increased.

Chapter V. Conclusions

An experimental investigation was carried out to determine the heat transport capabilities of an OHP with an MPCM slurry working fluid. Microtek Laboratories Inc's Nexttek37D and MPCM57D were analyzed to determine thermophysical properties. To produce peak heat transport, temperature ranges for the testing environments were selected around the PCM melting temperature range. A recirculating cooling bath temperature for Nexttek37D slurries was selected at 20°C because the experimental melting temperature of Nexttek37D is 39.47°C. Additionally, recirculating cooling bath temperature for MPCM57D slurries was selected at 40°C because the experimental melting temperature of MPCM57D is 60.52°C. OHP performance was optimally enhanced when the MPCM were at a weight concentration of 3% in the slurry. Most MPCM in water slurries yielded improvement over water working fluid in the OHP. The MPCM slurries generated the best results at a power level of 200 W. As the discrete power level increased, thermal conductance also increased.

References

1. Ma, H. B., Borgmeyer, B., Cheng, P., and Zhang, Y. (2008). “Heat Transport Capability in an Oscillating Heat Pipe,” *Journal of Heat Transfer*, *130*(8). https://doi.org/10.1115/1.2909081
2. Ando, M., Okamoto, A., Tanaka, K., Maeda, M., Sugita, H., Daimaru, T., and Nagai, H. (2018). “On-Orbit Demonstration of Oscillating Heat Pipe with Check Valves for Space Application,” *Applied Thermal Engineering*, 130, 552–560. https://doi.org/10.1016/j.applthermaleng.2017.11.032
3. Abela, M., Mameli, M., Nikolayev, V., and Filippeschi, S. (2022). “Experimental Analysis and Transient Numerical Simulation of a Large Diameter Pulsating Heat Pipe in Microgravity Conditions,” *International Journal of Heat and Mass Transfer*, 187, 122532. https://doi.org/10.1016/j.ijheatmasstransfer.2022.122532
4. Ji, Y., Ma, H., Su, F., and Wang, G. (2011). “Particle Size Effect on Heat Transfer Performance in an Oscillating Heat Pipe,” *Experimental Thermal and Fluid Science*, 35(4), 724–727. https://doi.org/10.1016/j.expthermflusci.2011.01.007
5. Davari, H., Goshayeshi, H.R., and Öztop, H.F. (2020). “Experimental Investigation of Oscillating Heat Pipe Efficiency for a Novel Condenser by Using Fe_3O_4 Nanofluid,” *J Therm Anal Calorim* 140, 2605–2614. https://doi.org/10.1007/s10973-019-09032-8
6. Ankursinh P. and Hardik M. Patel. (2014). “Experimental Analysis of Close Loop Pulsating Heat Pipe at Different Filling Ratio.” *IJEDR.* Vol. 2, Issue 2.
7. Ma, H. B., Wilson, C., Borgmeyer, B., Park, K., Yu, Q., Choi, S. U., and Tirumala, M. (2006). “Effect of Nanofluid on the Heat Transport Capability in an Oscillating

Heat Pipe," *Applied Physics Letters*, 88(14), 143116. https://doi.org/10.1063/1.2192971

8. Shi, W., and Pan, L. (2017). "Influence of Filling Ratio and Working Fluid Thermal Properties on Starting Up and Heat Transferring Performance of Closed Loop Plate Oscillating Heat Pipe with Parallel Channels," *Journal of Thermal Science*. https://link.springer.com/article/10.1007/s11630-017-0912-0
9. Hao, T., Ma, H., and Ma, X. (2019). "Experimental Investigation of a Three-Phase Oscillating Heat Pipe," *Journal of Thermal Science and Engineering Applications*, 11(6). https://doi.org/10.1115/1.4043090
10. Liu, X., Chen, Y., and Shi, M. (2013). "Dynamic Performance Analysis on Start-Up of Closed-Loop Pulsating Heat Pipes," *International Journal of Thermal Sciences*, 65, 224–233. https://doi.org/10.1016/j.ijthermalsci.2012.10.012
11. Zhou, Y., Cui, X., Weng, J., Shi, S., Han, H., and Chen, C. (2018). "Experimental Investigation of the Heat Transfer Performance of an Oscillating Heat Pipe with Graphene Nanofluids," *Powder Technology*, 332, 371–380.
12. Wang, Q., Rao, Z., Huo, Y., and Wang, S. (2016). "Thermal Performance of Phase Change Material/Oscillating Heat Pipe-Based Battery Thermal Management System," *International Journal of Thermal Sciences*, *102*, 9–16. https://doi.org/10.1016/j.ijthermalsci.2015.11.005
13. Zhao, J., Rao, Z., Liu, C., and Li, Y. (2016). "Experiment Study of Oscillating Heat Pipe and Phase Change Materials Coupled for Thermal Energy Storage and Thermal Management," *International Journal of Heat and Mass Transfer*, 99, 252–260. https://doi.org/10.1016/j.ijheatmasstransfer.2016.03.108

14. Li, Q., Wang, Y., Lian, C., Li, H., and He, X. (2019). “Effect of Micro Encapsulated Phase Change Material on the Anti-Dry-Out Ability of Pulsating Heat Pipes,” *Applied Thermal Engineering*, 159, 113854. https://doi.org/10.1016/j.applthermaleng.2019.113854
15. Zhao, J., Qu, J., and Rao, Z. (2018). “Thermal Characteristic and Analysis of Closed Loop Oscillation Heat Pipe/Phase Change Material (CLOHP/PCM) Coupling Module with Different Working Media,” *International Journal of Heat and Mass Transfer*, 126, 257–266. https://doi.org/10.1016/j.ijheatmasstransfer.2018.05.125
16. Heydarian, R., Shafii, M.B., and Rezaee Shirin-Abadi, A. (2019). “Experimental Investigation of Paraffin Nano-Encapsulated Phase Change Material on Heat Transfer Enhancement of Pulsating Heat Pipe,” *J Therm Anal Calorim*. 137, 1603–1613 (2019). https://doi.org/10.1007/s10973-019-08062-6
17. Hao, T., Ma, X., Lan, Z., Li, N., Zhao, Y., and Ma, H. (2014). “Effects of Hydrophilic Surface on Heat Transfer Performance and Oscillating Motion for an Oscillating Heat Pipe,” *International Journal of Heat and Mass Transfer*, 72, 50–65. https://doi.org/10.1016/j.ijheatmasstransfer.2014.01.007
18. Rittidech, S., and Wannapakne, S. (2007). “Experimental Study of the Performance of a Solar Collector by Closed-End Oscillating Heat Pipe (CEOHP),” *Applied Thermal Engineering*, 27(11-12), 1978–1985. https://doi.org/10.1016/j.applthermaleng.2006.12.005
19. Mangini, D., Mameli, M., Georgoulas, A., Araneo, L., Filippeschi, S., and Marengo, M. (2015). “A Pulsating Heat Pipe for Space Applications: Ground and Microgravity

Experiments," *International Journal of Thermal Sciences*, *95*, 53–63. https://doi.org/10.1016/j.ijthermalsci.2015.04.001

20. Burban, G., Ayel, V., Alexandre, A., Lagonotte, P., Bertin, Y., and Romestant, C. (2013). "Experimental Investigation of a Pulsating Heat Pipe for Hybrid Vehicle Applications," *Applied Thermal Engineering*, 50(1), 94–103. https://doi.org/10.1016/j.applthermaleng.2012.05.037
21. Sevilla, L. T., and Radulovic, J. (2021). "Investigation of Low Grade Thermal Energy Storage Systems with Phase Changing Materials," *Energy and Built Environment*, 2(4), 366–373. https://doi.org/10.1016/j.enbenv.2020.05.006
22. Shchukina, E. M., Graham, M., Zheng, Z., and Shchukin, D. G. (2018). "Nanoencapsulation of Phase Change Materials for Advanced Thermal Energy Storage Systems," *Chemical Society Reviews*, 47(11), 4156–4175. https://doi.org/10.1039/c8cs00099a
23. Faraj, K., Khaled, M., Faraj, J., Hachem, F., and Castelain, C. (2021). A Review on Phase Change Materials for Thermal Energy Storage in Buildings: Heating and Hybrid Applications," *Journal of Energy Storage*, 33, 101913. https://doi.org/10.1016/j.est.2020.101913
24. Peng, G., Dou, G., Hu, Y., Sun, Y., and Chen, Z. (2020). "Phase Change Material (PCM) Microcapsules for Thermal Energy Storage," *Advances in Polymer Technology*, 2020, 1–20. https://doi.org/10.1155/2020/9490873
25. Monroe, J. G., Kumari, S., Fairley, J. D., Walters, K. B., Berg, M. J., and Thompson, S. M., 2019, "On the Energy Harvesting and Heat Transfer Ability of a Ferro-

Nanofluid Oscillating Heat Pipe," International Journal of Heat and Mass Transfer, 132, 162–171. https://doi.org/10.1016/j.ijheatmasstransfer.2018.11.096

26. Pandey, H., and Kumar Gupta, N., 2022, "A Descriptive Review of the Thermal Transport Mechanisms in Mono and Hybrid Nanofluid-Filled Heat Pipes and Current Developments," Thermal Science and Engineering Progress, 31, 101281. https://doi.org/10.1016/j.tsep.2022.101281
27. Riehl, R. R., Murshed, S. M. S., 2022, "Performance Evaluation of Nanofluids in Loop Heat Pipes and Oscillating Heat Pipes," International Journal of Thermofluids, 14, 100147. https://doi.org/10.1016/j.ijft.2022.100147
28. Jin, H., Lin, G., Zeiny, A., Bai, L., Cai, J., and Wen, D., 2019, "Experimental Study of Transparent Oscillating Heat Pipes Filled with Solar Absorptive Nanofluids," International Journal of Heat and Mass Transfer, 139, 789–801. https://doi.org/10.1016/j.ijheatmasstransfer.2019.04.117
29. Faghri, A., and Zhang, Y. (2020). "Fundamentals of Multiphase Heat Transfer and Flow," https://doi.org/10.1007/978-3-030-22137-9
30. Rajabi Far, B., Mohammadian, S. K., Khanna, S. K., and Zhang, Y. (2015). Effects of Pin Tip-Clearance on the Performance of an Enhanced Microchannel Heat Sink with Oblique Fins and Phase Change Material Slurry," *International Journal of Heat and Mass Transfer*, 83, 136–145. https://doi.org/10.1016/j.ijheatmasstransfer.2014.11.082